



MEMS miniaturized low-noise magnetic field sensor for the observation of sub-millihertz magnetic fluctuations in space exploration

X. Manyosa^{a,d}, D. Roma-Dollase^{b,d}, M. Arqué^{b,d}, B. Bonastre^{b,d}, V. Jiménez^{a,d},
J. Ramos-Castro^{a,d}, J. Pons-Nin^{a,d}, V. Martín^{b,d}, J. Salvans-Tort^{b,d}, S. Gómez^{a,c}, A. Sanuy^{c,d},
J. Mauricio^{c,d}, D. Gascon^{c,d}, M. Nofrarias^{b,d}, M. Domínguez-Pumar^{a,d,*}

^a Universitat Politècnica de Catalunya, Jordi Girona 31, 08034 Barcelona, Spain

^b Institut de Ciències de l'Espai, Campus UAB, Carrer de Can Magrans sn, 08193 Cerdanyola del Valles, Spain

^c Universitat de Barcelona, ICCUB, Barcelona, Spain

^d Institut d'Estudis Espacials de Catalunya (IEEC), Gran Capita, 2-4, Ed. Nexus, 08034 Barcelona, Spain

ARTICLE INFO

Keywords:

Magnetometer
Magnetic field modulation
1/f noise

ABSTRACT

The objective of this paper is to show that, using magnetic field modulation with a MEMS resonator, it is possible to reduce the noise floor of a commercial Tunneling Magnetic Resistance by one order of magnitude, in the ultra-low frequency range. Low noise at this frequency range is a strong requirement in planetary or space exploration missions like LISA (Laser Interferometer Space Antenna), where the observed gravitational waves will be in the 0.1 mHz to 0.1 Hz range. It will be shown that the noise spectral amplitude after demodulation from 0.1 mHz to 100 mHz is well below the 100 nT/ $\sqrt{\text{Hz}}$ requirement for the future space-borne gravitational wave detector LISA – that we take as reference – being at 20 nT/ $\sqrt{\text{Hz}}$ at 0.1 mHz, and reaching an average 1.5 nT/ $\sqrt{\text{Hz}}$ at higher frequencies, from 100 mHz to 1 Hz.

1. Introduction

Measurement of magnetic fields is a key issue for many science objectives in space exploration. At the surface of planetary bodies, static magnetic fields are typically measured for studying remnant paleomagnetizations [1,2] and for identifying the presence of magnetized rocks below the surface [3]. In the area of planetary and minor bodies exploration, very low frequency magnetic field fluctuations appear on the surface of these bodies as a result of changes generated by the Interplanetary Magnetic Field (IMF), Solar wind, extreme UV radiation (EUV), or, alternatively, events generated by other planets (such as in the case of crossing another planet magneto-tail), [4–6]. All these phenomena trigger variations in the magnetic field at the surface of planets in a very low frequency range and can, additionally, induce currents at the cores of the bodies themselves. By studying the transfer functions between the external excitation and the induced magnetic fluctuations it is possible to study the conductivity of the core and even its morphology [5]. On the other hand, magnetic field fluctuations can generate disturbances in instruments where the signal to be retrieved is in the very low frequency range, as is the case of the Very Broad Band (VBB) seismometer onboard InSight, [4], where low frequency magnetic field fluctuations are a potential interference source on the seismic wave signal.

In parallel with all these applications, among fundamental physics missions, there are equally stringent requirements for magnetic sensing. This is the case for future space-borne gravitational wave detectors, as in the LISA mission (Laser Interferometer Space Antenna) [7], where magnetic fields on-board need to be carefully monitored given that its variation can induce spurious forces in the free-falling test masses on-board. The precursor LISA Pathfinder mission already carried a magnetic diagnostics subsystem composed by four fluxgate magnetometers [8]. However, the permalloy core in these devices forced to locate them far from the sensitive location to avoid any potential magnetic back-action. Future space mission implementing atomic interferometers [9] would also encounter similar challenges as the ones in LISA, since the atom species proposed at the core of these experiments are highly sensitive to magnetic disturbances.

Despite this variety of research areas, there is a common need for high precision, compact and low power consumption magnetic monitoring systems which, at the same time, should reach an extremely stable measurement regime. Typically, we refer to this ultra-stable regime as that involving fluctuation in the range from 10^{-5} Hz or 10^{-4} Hz, to 0.1 Hz. This range represents a significant challenge for sensors and electronics because, in those low frequencies, the intrinsic

* Corresponding author at: Institut d'Estudis Espacials de Catalunya (IEEC), Gran Capita, 2-4, Ed. Nexus, 08034 Barcelona, Spain.

E-mail addresses: nofrarias@ice.csic.es (M. Nofrarias), manuel.dominguez@upc.edu (M. Domínguez-Pumar).

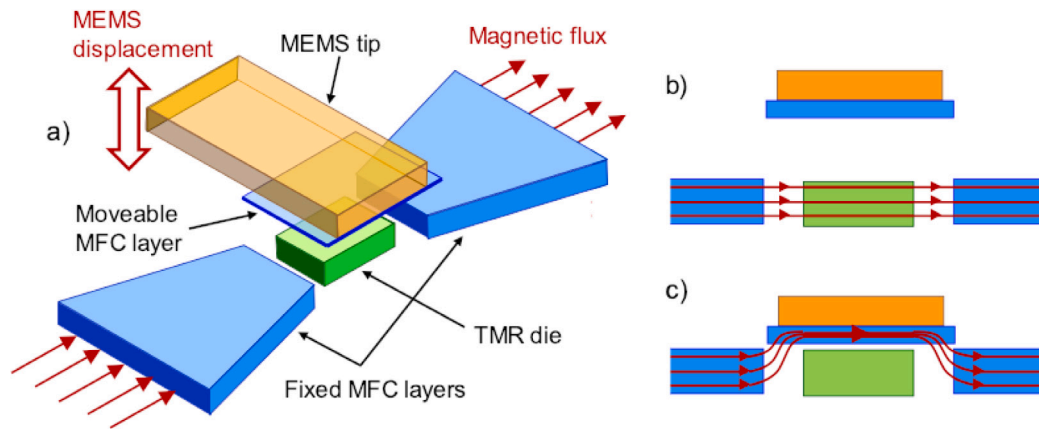


Fig. 1. (a) General concept of the sensor. Two static MFC (Magnetic Field Concentrator) layers are placed near the TMR to increase the sensor sensitivity. A MEMS resonator is placed over the TMR with a high- μ material (movable MFC, or MMFC) placed at its tip. (b) MEMS resonator is at the UP position above the TMR; local magnetic field at the TMR is almost undisturbed. (c) MEMS resonator is at the DOWN position above the TMR; the high- μ material placed on the resonator decreases the local magnetic field at the TMR. Color coding: μ -metal is depicted in blue, the TMR sensor in green, and the MEMS in orange.

$1/f$ noise is the predominant contribution when trying to have a low noise floor.

A standard approach to tackle the difficulty imposed by the $1/f$ noise generated at the magnetic sensor head is to implement a signal modulation scheme that implicitly shifts the measurement to higher frequencies, where it is possible to avoid the $1/f$ noise usually dominating the sensor response. Typically, this is achieved by placing a high permeability material attached to a resonator near the sensor head, therefore modulating its local magnetic field, and up-converting the signal to higher frequencies. An extensive literature can be found focused on the implementation of magnetic field modulations, [10–16], but most of the works present amplitude spectral densities at frequencies well above the inferior limit of these missions (e.g. 1 Hz), and the ones that extend to those low frequencies are not miniaturized [16]. Therefore, the main objective of this work is to extend the experimental results obtained with this technique to this frequency range, in particular analyzing the possibility of fulfilling the stringent requirements of the LISA mission.

In this work, a high permeability material is attached to a MEMS resonator modulating the local magnetic field at a Tunneling Magnetoresistance (TMR). Furthermore, since we address the very low frequency regime, we impose high stability requirements on both our acquisition system and the lab environment. As it has been mentioned before, the objective of this paper is to show that it is possible to use this modulation technique in the ultra-low frequency range needed in space exploration. The output of our work is a miniaturized and low consumption magnetometer prototype, reaching a noise amplitude spectral density (ASD) of $20 \text{ nT}/\sqrt{\text{Hz}}$ at 0.1 mHz and decreasing down to a floor noise of $1.5 \text{ nT}/\sqrt{\text{Hz}}$ at higher frequencies, from 100 mHz to 1 Hz.

2. Sensor description

As mentioned in the Introduction, the system implements magnetic field modulation on a Tunneling Magnetoresistance (TMR). Fig. 1 shows a scheme of the concept. The TMR is placed between two high-permeability static layers in order to increase sensitivity (acting as Magnetic Flux Concentrators, MFC). A MEMS cantilever resonates over the TMR, which is a bare die of a TMR9001 from MultiDimension. The presence of a high magnetic permeability material on the tip of the mechanical system over the TMR allows the modulation of the local field. This part of the structure, including this layer, is therefore called Moveable MFC (MMFC). By exciting the MEMS at its resonance, the low-frequency content of the magnetic field can be modulated to frequencies where the $1/f$ noise fades, to be afterwards demodulated computationally, therefore avoiding the presence of the $1/f$ noise contribution coming from the magnetic sensor, the TMR.

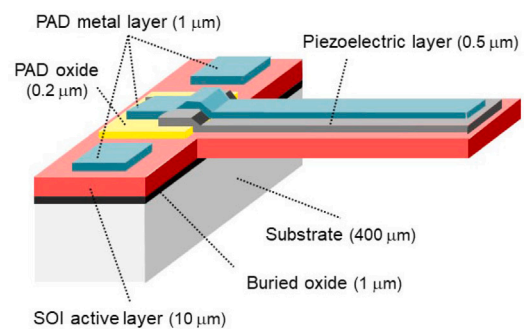


Fig. 2. 3D schematic of the MEMS resonators fabricated with PiezoMUMPS technology.

2.1. MEMS design and sensor assembly

The MEMS resonators have been fabricated using PiezoMUMPS technology from MEMSCAP. This technology uses crystalline silicon ($10 \mu\text{m}$ thick Silicon-On-Insulator, SOI) as structural material and AlN ($0.5 \mu\text{m}$ thick) as piezoelectric material. To maximize the oscillation amplitude, the resonators are cantilevers (4 mm long and 0.75 mm or 1 mm wide). The structure of the MEMS resonator is shown in Fig. 2. The MMFC is a sheet of μ -metal with $1.25 \times 1 \text{ mm}$ area and $25 \mu\text{m}$ thick that is bonded onto the tip of the MEMS cantilever using a thin layer of epoxy.

In order to have information on the expected frequency behavior of the MEMS cantilevers designed, simulations of the mechanical structure with a commercial Finite Element Method (FEM) software have been carried out. The results of these simulations, shown in Figure 3, indicate that the frequency of the first resonance mode is 964 Hz . This resonance frequency drops to 254 Hz when the MMFC is added on the tip of the cantilever, as reported in the same Figure.

The experimental measurements carried out with the MEMS resonators give results that match with those predicted in the simulations. Thus, the resonance frequency of the first mode measured before placing the MMFC layer is always around 900 Hz . Once the MMFC layer has been added, this frequency decreases to $240\text{--}280 \text{ Hz}$. Let us also note that the quality factor of the resonators is approximately $Q=100$ at atmospheric pressure and $Q = 900$ at low pressure (10^{-3} mbar), which implies a greater oscillation amplitude in environments such as space.

The sensor assembly consists of aligning two printed-circuit boards (PCB). The first PCB provides physical support and electrical connectivity for the MEMS resonator, whereas the second PCB provides physical

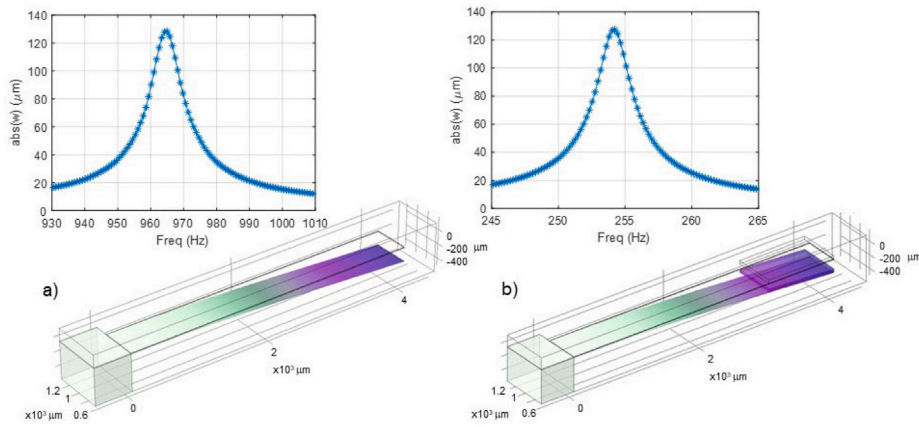


Fig. 3. FEM simulation results of the first mechanical resonance of a MEMS cantilever, without (a) and with (b) the MMFC placed on its tip. A quality factor of 100 (atmospheric conditions) and a thickness of 50 μm for the MMFC-epoxy structure have been considered. The first eigenfrequency is 965 Hz in (a) and 254 Hz in (b). Note that a longitudinal symmetry condition has been applied along the cantilever to reduce the computational load.

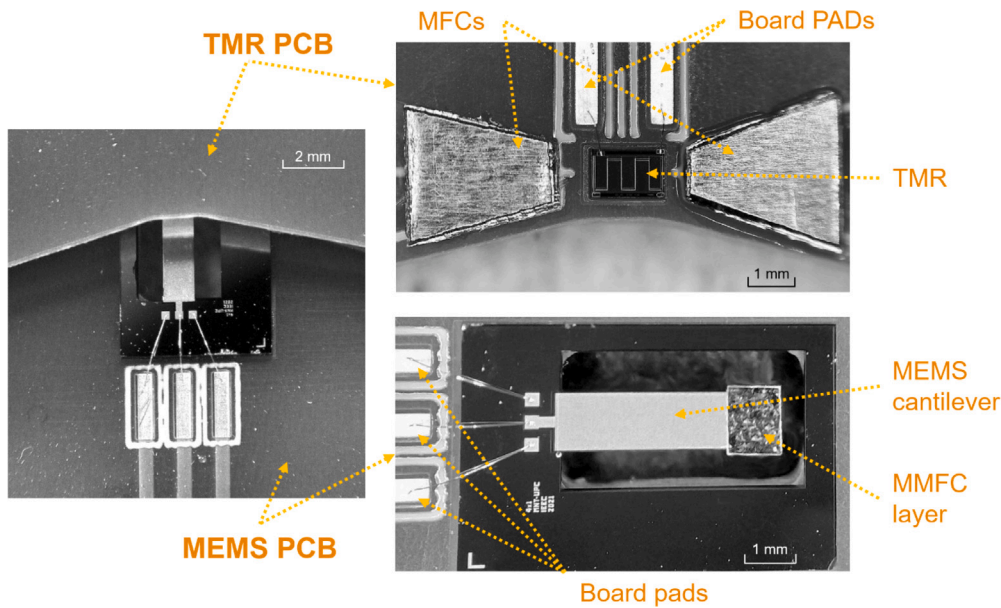


Fig. 4. Photographs of the sensor prototype developed in this work. Left: general view of the prototype, showing the MEMS (down) and the TMR (up-capsized) boards. Right-top: active area of the TMR board. Right-bottom: active area of the MEMS board.

support for the TMR and the MFCs and electrical connectivity for the TMR. An optical micropositioner is used to perform the alignment as accurately as possible. The modulation efficiency of the magnetic field is taken as a figure of merit. It is calculated as the quotient of the sensitivity of the system under modulation, and the AC sensitivity without modulation, [11], before the MEMS resonator is placed near the TMR in order not to count the possible insertion losses. The sensitivity of the system under modulation is defined as the ratio of the output variation under modulation and the external magnetic field.

For these measurements, a Helmholtz coil is used to generate a known magnetic field at a given frequency. Then, the alignment of the TMR and MEMS boards is adjusted to maximize the modulation efficiency. Once an optimal positioning has been achieved, the PCBs are fixed by inserting quartz rods through holes in the PCBs and, afterwards, bonding the system with epoxy. Figure 4 shows different pictures of the sensor prototype implemented, including detailed views of both the MEMS and the TMR boards. Let us note that the volume of the sensor is very small, approximately $20 \times 20 \times 7$ mm.

2.2. Ultra low-noise acquisition electronics

The design of the low-noise acquisition and control electronics takes advantage of previous developments specifically designed to achieve a high performance in the millihertz frequency regime [17,18]. As we will show, imposing a low noise requirement in the millihertz band has an important impact in different stages of the acquisition chain. The acquisition and control electronics excites the first resonance of the MEMS and acquires the modulated TMR signal by using a Wheatstone bridge, where in one of the arms is the TMR element. A functional block diagram of the control and acquisition system can be seen in Fig. 5. The total gain of the Front End Electronics (FEE) is 41, which makes the additive noise contribution of the other elements of the chain placed afterwards negligible with regards to the difference amplification input stage. This difference amplification stage is implemented using a CMOS input amplifier to minimize the current noise contribution due to the high nominal resistance of the sensor arm. The reference arm of the Wheatstone bridge is made of high-stability resistors with ultra-low

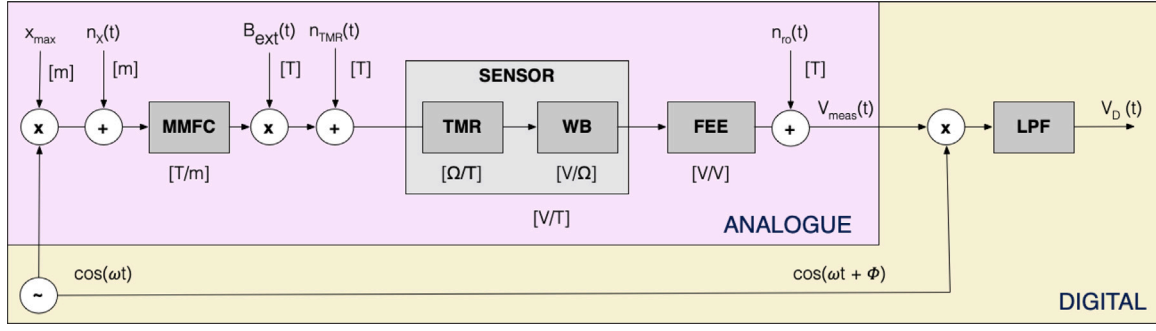


Fig. 5. Scheme of the detection model. The main elements are the Moveable Magnetic Flux Concentrator (MMFC), in our case a MEMS cantilever, that translates its displacement into a modulated magnetic field as sensed by the Tunneling Magnetoresistance (TMR) sensor. Together with the Wheatstone bridge (WB), these converts the modulated signal into the analogue signal read-out by the front-end electronics (FEE) and finally filtered through a Low-Pass Filter (LPF). More details in the text.

temperature coefficients and two order of magnitude lower resistance values to minimize its thermal noise contribution. Overall, considering the most sensitive manufactured sensor, and the saturation limits of the acquisition electronics, the minimum magnetic measurement range of the whole system is about $\pm 75 \mu\text{T}$, well above the requirements of missions like LISA, and high enough to allow on-ground testing without canceling the Earth magnetic field.

2.3. Noise model

We will introduce a noise model to take into account the different stages of the modulation scheme. As we will show latter, this analysis will turn up to be useful in identifying the relevant design parameters in our system and draw conclusions from our results. The starting point is the description of the magnetic field measured by the TMR sensor, B_{TMR} , as a linear relation between measured magnetic field and displacement of the MEMS cantilever. We will consider, x , such as

$$\begin{aligned} B_{TMR}(x = x_{max}) &= \alpha B_{ext} \\ B_{TMR}(x = -x_{max}) &= \gamma B_{ext} \end{aligned} \quad (1)$$

Where we considered that $x = 0$ is the rest position of the MEMS resonator, and where $x = x_{max}$ corresponds to the farthest point away from the sensor that the MEMS can reach and $x = -x_{max}$ is the closest the MEMS can get to the TMR. In this case, α is the insertion loss coefficient (i.e. accounting for a partial distortion of the magnetic flux when introducing the cantilever with the high permeability layer placed) and γ a modulation loss coefficient (i.e. accounting for a non-total modulation of the magnetic field). Notice that one can recover an ideal case by making $\alpha = 1$ and $\gamma = 0$.

This yields the simple model of the measured magnetic field at the sensor, given by

$$B_{TMR}(t) = B_{ext}(t) \left(\frac{\alpha + \gamma}{2} + \frac{\alpha - \gamma}{2x_{max}} x(t) \right) + n_{TMR}(t) \quad (2)$$

where n_{TMR} is the contribution of the sensor noise, and $x(t)$ stands for the vertical displacement of the cantilever tip. The previous equation is implicitly carrying the modulation introduced by the cantilever motion

$$x(t) = x_{max} \cos(\omega_m t + \phi) + n_x(t) \quad (3)$$

being ϕ a phase to account for any lack of coherent detection and phase introduced by the MEMS resonator, and n_x stands for any displacement noise at the cantilever. For the simplicity, we will consider ϕ to be zero, which can be always achieved by calibrating the system and compensating its phase delay.

A figure of merit of the quality of our system will be the modulation depth that we define, in the previous terms, as

$$m = \frac{B_{max} - B_{min}}{B_{nf}} = \frac{\alpha B_{ext} - \gamma B_{ext}}{B_{ext}} = \alpha - \gamma \quad (4)$$

where B_{nf} is the magnetic field at the TMR in the absence of the MMFC and MEMS resonator (i.e., without the insertion losses). The ideal case corresponds in this notation to $m = 1$, or expressed as a percentage, $m = 100\%$.

The previous definition of the modulation depth allows us to rewrite the measured magnetic field as

$$B_{TMR}(t) = B_{ext}(t) \left(\frac{\alpha + \gamma}{2} + \frac{m}{2x_{max}} x(t) \right) + n_{TMR}(t) \quad (5)$$

an expression that describes the measured magnetic field at the sensor in terms of the displacement of the cantilever tip and the modulation depth. Our noise analysis needs to consider as well those disturbances arising in the acquisition and signal conditioning chain. To do so and following our detection functional scheme, Fig. 5, we need to add the sensor and noise read-out contribution, $n_{ro}(t)$, which leads to

$$V_{meas}(t) = H_{TMR} B_{TMR}(t) + n_{ro} \quad (6)$$

where, to ease the notation, we are not expanding the whole dependency in the expression. H_{TMR} contains the sensor transfer function which we would express by means of the sensor sensitivity, α_S and the front-end electronics gain, α_G , i.e. $H_{TMR} = \alpha_S \alpha_G$. In Fig. 5, we made explicit these two contributions in the sensor scheme.

It will suffice to restrict ourselves to the first order, and gather the gain factors of sensor and bridge, which for small variations of the TMR can be considered linear, into the gain α_S . Nevertheless, we consider worth introducing here this discussion since in the experimental characterization that we present in the next section we will express the response of the TMR in terms of the sensor resistance.

The demodulation is digitally performed and the output data low-pass filtered to keep only the base-band signal. From this demodulated and filtered measurement, $V_D(t) = LPF\{V_{meas}(t) \cos(\omega_m t)\}$, the magnetic field, after re-scaling by the sensitivity factor, can be extracted as:

$$\begin{aligned} B_{meas}(t) &= \frac{V_D(t)}{(m \alpha_S \alpha_G)/4} = \\ &= B_{ext}(t) + 2 \frac{[B_{ext} n_x]_c(t)}{x_{max}} + \\ &+ \frac{4}{m} n_{TMR,c}(t) + \frac{4}{m} \frac{n_{ro,c}(t)}{\alpha_S \alpha_G} \end{aligned} \quad (7)$$

where $[B_{ext} n_x]_c(t)$, $n_{TMR,c}(t)$, and $n_{ro,c}(t)$ stand for the noise terms after low-pass filtering, i.e.:

$$\begin{aligned} [B_{ext} n_x]_c(t) &= LPF[B_{ext}(t) n_x(t) \cos(\omega_m t)] \\ n_{TMR,c}(t) &= LPF[n_{TMR}(t) \cos(\omega_m t)] \\ n_{ro,c}(t) &= LPF[n_{ro}(t) \cos(\omega_m t)] \end{aligned} \quad (8)$$

The factor 4 in Eq. (7) comes from the modulation of the magnetic field itself (this generates a factor 1/2) and the demodulation factor 1/2 introduced by the multiplication by the carrier and the LPF. These

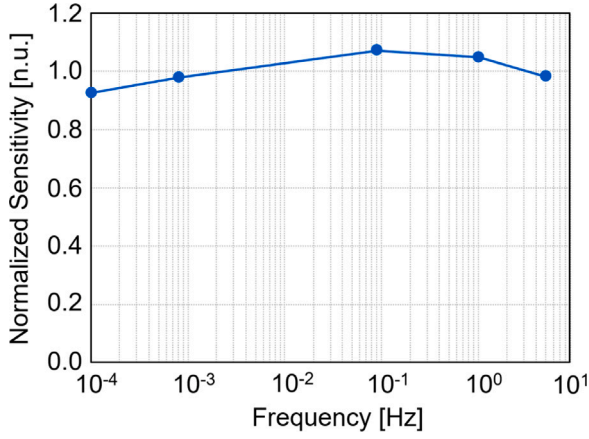


Fig. 6. Normalized sensitivity of the complete system, excited with a magnetic field at different frequencies in the range 0.1 mHz–5 Hz.

noise signals represent the respective noise components at the carrier frequency shifted after demodulation.

The resulting spectrum of fluctuations associated to the measured magnetic field can be expressed as:

$$S_{B_{meas}}(\omega) = S_{B_{ext}}(\omega) + 2 \frac{S_{B_{ext}, n_x}}{x_{max}^2}(\omega') + \frac{8}{m^2} \left[S_{TMR}(\omega') + \frac{S_{ro}(\omega')}{\alpha_S^2 \alpha_G^2} \right] \quad (9)$$

where, because of the applied modulation, we are evaluating the noise terms at $\omega' = \omega + \omega_m$. The noise cross terms have vanished since they represent jointly independent processes. With regard to the S_{B_{ext}, n_x} term, this disturbance could arise, for instance, if temperature fluctuations would modify the cantilever displacement. This effect, already described in the literature [19], goes beyond the scope of our analysis so we will restrict ourselves to the following expression:

$$S_{B_{meas}}(\omega) = S_{B_{ext}}(\omega) + \frac{8}{m^2} \left[S_{TMR}(\omega') + \frac{S_{ro}(\omega')}{\alpha_S^2 \alpha_G^2} \right] \quad (10)$$

where we assume that our system has no implicit phase introduced by the demodulation process ($\phi = 0$) and that, as it has been mentioned before, there is no noise that correlates the magnetic field with the displacement of the cantilever tip, i.e. $S_{B_{ext}, n_x}(\omega) = 0$. The ideal situation will be that the electronics noise and the sensor noise are low enough with regards the magnetic field fluctuations. Since the gain and sensitivity of our system is high and its intrinsic noise low, the electronics noise contribution will be already below our requirement. For the sensor noise, the only feasible way to reduce its noise contribution will be to increase the frequency of the modulation signal enough, while at the same time reducing the white noise floor at those frequencies.

3. Experimental results

Extensive measurements were carried out to characterize the complete system in the required low frequency range. The complete system was placed in a mu-metal chamber, used to shield the sensor from external magnetic field disturbances, while both sensors and mu-metal chamber were placed inside a vacuum chamber. Inside the mu-metal chamber, a coil allowed controlled magnetic injections that we used for calibration and characterization purposes.

During this work, the sensitivity of the system to an external field was measured at 5 Hz for convenience. However, it is important to ensure that this sensitivity is approximately the same as in the range from 0.1 mHz to 1 Hz. Therefore, sensitivity measurements at different frequencies were performed. The results, shown in Fig. 6, indicate a

maximum deviation of 7.5% at 0.1 mHz. This small deviation can be due to environmental factors affecting these very slow measurements, such as temperature and pressure drift. Therefore, we can assume that the sensitivity is fairly constant with frequency.

The quality factor and resonant frequency were measured by the impedance analyzer (Hioki IM3590). The characterization in Fig. 7(a) shows a resonance at 267.9 Hz. We used the calibration coil to explore the response in the TMR sensors. As seen in Fig. 7(b), the sensor shows a linear dependence in the $\pm 10 \mu\text{T}$ evaluated range. The results in the plot show the mean value of both a negative to positive sweep and the inverse. In doing so, we tried to evaluate any potential hysteresis in the response of the sensor, which we did not observe.

TMR sensors can show a non-zero response in a situation of zero applied magnetic field. This can either be attributed to a remnant magnetic field from the sensor that will add upon the applied external field or, alternatively, to a manufacturing tolerance of the nominal resistance of the sensor at zero field with regard to the fixed resistance at the Wheatstone bridge. We took advantage of the characterization in Fig. 7(b) to derive the resistance of the sensor at zero field. Indeed, from the response obtained, we can extrapolate that for an applied zero external field, the response of the sensor has an equivalent offset bias of 100 nT. Following [10], for the rest of characterization runs we subtracted this value for the applied external magnetic field to then express our results in terms of the *modified* magnetic field applied to our TMR sensor. We also want to stress here that, in our characterization, we express the response of our sensor in terms of the variation of the resistance instead of the voltage response, as appears in other works in the literature. We consider the former a more natural magnitude since the latter can potentially mask dependencies that would be attributed to the non-linearity of the Wheatstone bridge with a single sensor than to the sensor itself.

In order to evaluate the device sensitivity, we use the coil in our setup to inject a magnetic signal at 5 Hz to then compare the amplitude of this modulation before placing the MEMS structure, with the amplitude of the modulated components (at 267.9 ± 5 Hz), once the MEMS has been positioned.

In Fig. 7(c) we show the device sensitivity for different DC magnetic fields. The sensitivity is expressed as the ratio of measured sensor resistance with respect the applied AC modulated magnetic field. We obtain a sensitivity around $90 \Omega/\mu\text{T}$ with the system without applying a modulation with the MEMS. The relative change of this value when varying the applied magnetic field in the range $[-10 \mu\text{T}, 10 \mu\text{T}]$ is 3.8%. The sensitivity reduces to $8.2 \Omega/\mu\text{T}$ when applying the modulation/demodulation scheme described in the previous section. Similarly, we can express the efficiency of our resonant device in modulating the magnetic field by means of the modulation depth. To that end, we compute the ratio of amplitude of the demodulated AC signal compared to the original signal at the modulated frequency. The results in Fig. 7(d) show a nearly constant value close to 36%. Despite not having a large modulation depth, this value is high enough to substantially increase the low frequency performance of our magnetic measurement as we show in the following Fig. 8.

The low frequency performance of the device was evaluated in the same setup with the mu-metal chamber inside a vacuum chamber. In this case, no magnetic field was applied but instead the system was left free running. First, without having placed the MEMS and MMFC, and therefore evaluating the native noise performance of the TMR sensors, and afterwards, with the amplitude obtained modulating with the MMFC, and demodulating computationally afterwards. In Fig. 8 we compare these two runs. To do so we have expressed the measured voltage fluctuations into equivalent magnetic noise by means of the device sensitivity, as previously described. Without modulation, at 0.1 mHz, the noise floor is approximately $200 \text{ nT}/\sqrt{\text{Hz}}$. When the sensor is being modulated by the MEMS, and after demodulating the recorded signal, the noise from 0.1 mHz to 100 mHz is well below the $100 \text{ nT}/\sqrt{\text{Hz}}$ requirement for LISA – that we take as reference – being at

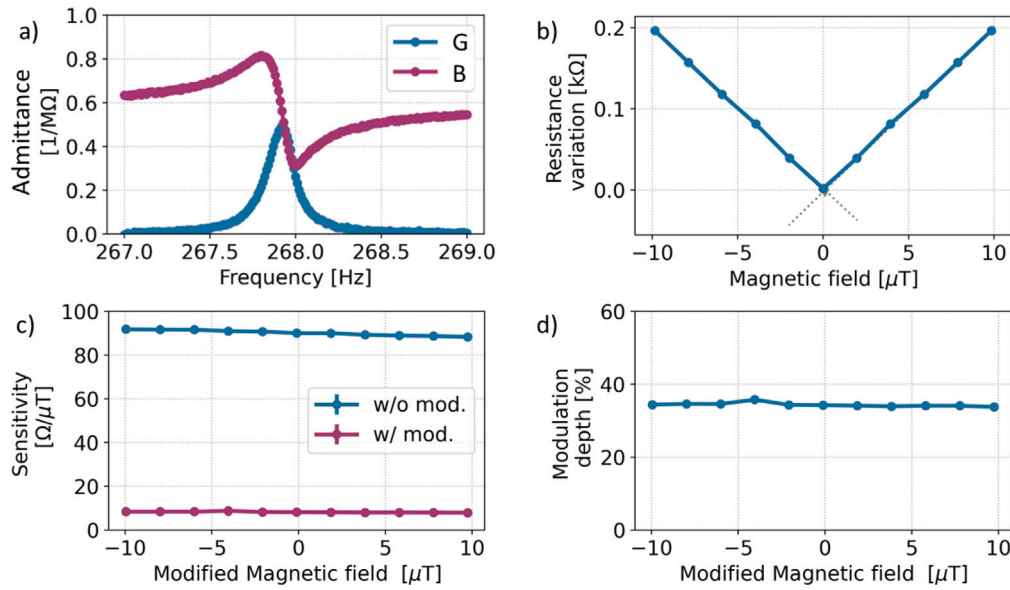


Fig. 7. Characterization of the magnetometer. From top to bottom, left to right: (a) Impedance characteristic curves of MMFC showing the Conductance (G) and Susceptance (B). (b) Amplitude of the modulation of the resistance at the carrier frequency for different DC magnetic fields. (c) Sensitivity with (w/) and without (w/o) modulation at different modified magnetic fields (different DC magnetic fields) (d) Modulation efficiency at different modified magnetic fields.

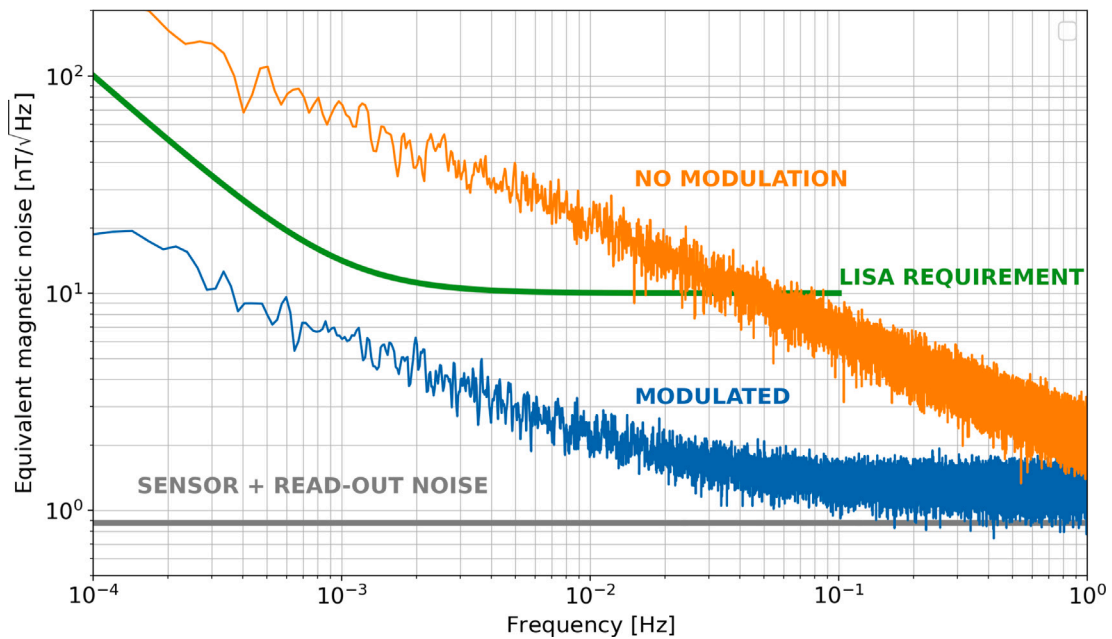


Fig. 8. Comparison between the noise floor measurement of the TMR with and without implementing magnetic field modulation. The amplitude spectral density of the recorded signal, after demodulation, presents a noise at 0.1 mHz of approximately 20 $\text{nT}/\sqrt{\text{Hz}}$. At higher frequencies, the floor noise reaches 1.5 $\text{nT}/\sqrt{\text{Hz}}$.

Table 1
Comparison of the developed MEMS magnetometer with other miniaturized magnetometers.

	This work	Bare die TMR from this work	Micro fluxgate sensors [20]	Hall-effect with MFCs [21]	AMR [22]	GMR [23]	TMR COTS [24]
Size/sensor [mm]	$20 \times 20 \times 7$	1×1.5	10×3	20×20	$5 \times 5 \times 1.5$	$1.8 \times 6.2 \times 5$	$6 \times 6 \times 0.75$
Num of sensing axis	1	1	1	1	1	3	1
Range [mHz]	$[0.1, 10^3]$	$[0.1, 10^3]$	$[5, 10^4]$	$[10, 10^4]$	$[0.1, 10^4]$	$[500, 10^7]$	$[100, 10^5]$
$S_b^{1/2}(f)$ [$\text{nT}/\sqrt{\text{Hz}}$]							
$f = 0.1$ mHz	20	300	-	-	4	-	-
$f = 1$ mHz	8	70	-	-	0.9	-	-
$f = 10$ mHz	2.5	20	0.4	0.1	0.2	-	-
$f = 100$ mHz	1.5	7	0.11	0.02	0.1	-	0.5
$f = 1$ Hz	1.5	3	0.11	0.01	0.1	10	0.15

Table 2
Comparison of the developed MEMS magnetometer to existing sensors for space exploration.

	This work	LISA pathfinder fluxgate [8]	Insight fluxgate [4]	Messenger fluxgate [25,26]	Galileo fluxgate [27–30]	Venus Pioneer fluxgate [31–33]
Size/sensor [mm]	20 × 20 × 7	35.1 × 32.3 × 82.6	75 × 74 × 52	81 × 48 × 46	81 ∅ 160 len.	67 × 67 × 42
Num of sensing axis	1	3	3	3	3	3
Range [mHz]	[0.1, 1000]	[1, 1000]	[10, 20000]	[10, 10000]	[0.1, 1000]	[30, 300]
$S_B^{1/2}(f)$ [nT/√Hz]						
$f = 0.1$ mHz	20	–	–	–	–	0.3
$f = 1$ mHz	8	10	–	–	–	0.1
$f = 10$ mHz	2.5	10	0.1	–	0.2	0.03
$f = 100$ mHz	1.5	10	0.1	–	–	0.01
$f = 1$ Hz	1.5	10	0.1	0.02	0.03	–

20 nT/√Hz at 0.1 mHz, and reaching an average 1.5 nT/√Hz at higher frequencies, from 100 mHz to 1 Hz.

The plateau at higher frequencies must be attributed to either read-out or sensor noise, which corresponds respectively, to the second and third term of our noise model in Eq. (10). We evaluate the sensor noise at the modulation frequency by taking the non-modulated noise spectrum in Fig. 8 at 267.9 Hz obtaining $S_{TMR}^{1/2}(\omega') \simeq 0.1$ nT/√Hz. The read-out noise, expressed as voltage noise at the input of the FEE, is $\frac{1}{\alpha_G} S_{ro}^{1/2}(\omega') = 20$ nV/√Hz [18]. This can be translated to equivalent magnetic noise as $\frac{1}{\alpha_S \alpha_G} S_{ro}^{1/2}(\omega') \simeq 0.05$ nT/√Hz, where in the previous steps we are considering $\alpha_G = 41$ as the read-out gain and $\alpha_S = 400$ V/T as the sensor sensitivity. Taking into account the modulation depth we get an estimate of $\simeq 0.9$ nT/√Hz floor noise coming from both sensor and read-out electronics, i.e. the last two terms in Eq. (10). This estimate is slightly below our measurement in Fig. 8, which represents an excess noise with respect our model that we attribute to noise sources present in our setup but not included in our model. Given that the mu-metal shield is suppressing the environmental magnetic fluctuations, the remaining 1/f excess noise at low frequencies can be attributed to different sources. In this very low frequency regime, it is usual to find coupling to temperature fluctuations [34] either through the temperature coefficient of the elements of the setup, the read-out electronics or the sensor itself. Also, the oscillator phase noise could couple into our modulation process and induce a similar increase in the low frequency band.

4. Conclusions

In the current work we have successfully proofed a MEMS-based modulation scheme for magnetic sensing in the low frequency regime. Further studies will follow to characterize the low frequency noise spectrum dependencies.

We have shown that a magnetic field modulation scheme can be successfully implemented to achieve a very low noise floor 20 nT/√Hz in the ultra-low frequency, i.e. sub-millihertz range, currently required for a wide variety of space mission that span areas from planetary exploration to fundamental physics.

This specification is, for instance, compatible with the monitoring of fluctuations of the Interplanetary Magnetic Field in the frequency range of interest for a space-borne gravitational wave detector such as LISA. By using a MEMS resonator with a commercial MEMS technology and a commercial TMR it is possible to fabricate a low cost miniaturized sensor fulfilling these stringent requirements.

Nevertheless, the technology chosen to implement the miniaturized magnetic field sensor described in this work is not, a priori, the only possible one. Thus, it is convenient to make here a comparison with other state-of-the-art sensing strategies, which can work in very low frequency ranges and are potentially usable in space applications. This comparison with alternative strategies is made in Table 1. For instance, micro fluxgate sensors, [20] present a noteworthy example of this technology with a noise floor of 110 pT/√Hz at 1 Hz and 0.4 nT/√Hz

at 10 mHz. Hall-effect-based magnetic sensors are widely used due to their compatibility with low-cost CMOS technology. Despite the relatively higher noise level compared with other MEMS magnetometers (25 μT/√Hz at 1 Hz in [35]), they have been used in conjunction with MFCs in [21] to reach noise levels of 0.1 nT/√Hz at 10 mHz. Furthermore, a wide range of operating temperatures (over 600 K) is available [36]. AMR sensors (Anisotropic Magneto Resistance) can provide both high sensitivity and a lower manufacturing cost than traditional fluxgate sensors. However, this type of sensors usually saturates at magnetic fields under the mT level, and they need often and complex desaturation procedures [37]. As an example, the noise level of the AMR studied in [22] is 4 nT/√Hz at 0.1 mHz. Giant Magneto-Resistance (GMR) sensors are sensitive up to 100 mT, and can work at high temperatures. However, GMR sensors can become permanently unusable when large (~ 1 T) magnetic fields are applied [38]. As an example, the COTS AAL002 [39] used in [23] has a noise of 10 nT/√Hz at 1 Hz. TMR sensors surpass the performance of the previously described miniaturized magnetic sensors in terms of sensitivity, temperature coefficient, power consumption, linearity and noise floor level [40]. For instance, the COTS TMR9112 [24] has a noise of 150 pT/√Hz at 1 Hz. And the bare die TMR used in this work, without modulation, has a noise of 300 nT/√Hz at 0.1 mHz and 3 nT/√Hz at 1 Hz, as it can be seen in Fig. 8. These superior attributes are the reasons why a TMR was chosen to act as the magnetic field measuring unit in the system described in this work. To the best of the authors' knowledge, other magnetic field modulation systems employing TMRs [10,11,41,42] have not targeted the ultra-low frequency range aimed here, at 0.1 mHz.

The magnetometer system developed in this work is a highly precise, low noise and miniaturized alternative for space applications. To this effect, let us now compare it with other magnetic sensors used in previous space missions. Table 2 shows a comparison between the results obtained in this work and sensors used in different missions. A comparison between the performance of our sensor and the magnetometers used in the missions as LISA Pathfinder [8], Insight [4], Messenger [25,26], Galileo [27–30] and Venus Pioneer [31–33], can be seen in Table 2. As shown, all of them are fluxgate sensors. We notice that the noise floor at different frequencies is close to the ones provided by the other sensors. Even though the sensor prototype of this work only has one sensing axis, it is the only one that can be fully miniaturized, it has a size of 20 × 20 × 7 mm, it is the 3% of the volume of the smallest one (LISA Pathfinder fluxgate), which means that if three sensors are used (one per axis), the total size would still be dramatically smaller than the other sensors.

The noise amplitude spectral density at very low frequencies of sensors in some missions is not always available, but some information can be found. For example, the MAG instrument on MAVEN [43,44] had an intrinsic noise of 15 pT, the MAG/ER on the Mars Global Surveyor [30,45,46] had an instrumental noise level of 0.5 nT, the Cassini magnetometer [47,48] had a noise of 5 pT/sqrt(Hz) at 1 Hz, and the Lunar Surface Magnetometer used on the Apollo missions 12, 15 and 16 [49,50], had a resolution of 0.2 nT.

Furthermore, it must be noted that the white noise limit at higher frequencies could be easily improved by sacrificing part of the wide range we currently have (± 75 uT) and increasing the gain of the read-out electronics. Finally, it is worth emphasizing that gaining one order of magnitude by modulating the magnetic field, instead of directly using the TMR, is essential for fulfilling the sensor requirements.

Being able to miniaturize the device provides two relevant advantages. First, it implies a substantial reduction of the power budget, which is critical in the framework of scientific space missions. The usage of a MEMS based magnetometer would typically reduce down to the milliwatt range a power consumption figure that is typically in the watt range for fluxgates. Second, for applications aimed at monitoring highly sensitive payloads, as in the case of fundamental physics missions, the magnetic back action effect, i.e. the effect due to the intrinsic magnetic field produced by the sensor, would be drastically reduced. The combination of these two advantages would enable magnetic monitoring solutions in these space missions which could take the shape of networks of sensors instead of a single device, a feature that would greatly improve the identification and diagnostic tasks on-board.

CRedit authorship contribution statement

X. Manyosa: Writing – review & editing, Writing – original draft, Investigation, Formal analysis, Data curation. **D. Roma-Dollase:** Writing – review & editing, Writing – original draft, Investigation, Formal analysis, Data curation. **M. Arqué:** Investigation. **B. Bonastre:** Investigation. **V. Jiménez:** Investigation. **J. Ramos-Castro:** Investigation. **J. Pons-Nin:** Investigation. **V. Martín:** Software, Investigation. **J. Salvans-Tort:** Investigation. **S. Gómez:** Investigation. **A. Sanuy:** Investigation. **J. Mauricio:** Investigation. **D. Gascon:** Investigation. **M. Nofrarias:** Writing – review & editing, Writing – original draft, Supervision, Methodology, Investigation, Funding acquisition, Formal analysis, Conceptualization. **M. Domínguez-Pumar:** Writing – review & editing, Writing – original draft, Supervision, Methodology, Investigation, Funding acquisition, Formal analysis, Conceptualization.

Declaration of competing interest

The authors declare that they have no known competing financial interests or personal relationships that could have appeared to influence the work reported in this paper.

Data availability

Data will be made available on request.

Acknowledgments

This work has been partially funded by Fundació I-CERCA, Spain through IEEC's internal seed funding project MELISA, and by MICINN, grant no. PID2019-106515GB-I00. This work was also partially supported by the program Unidad de Excelencia María de Maeztu, Spain CEX2020-001058-M.

References

- [1] D. Herčík, et al., The MASCOT magnetometer, *Space Sci. Rev.* 208 (1) (2017) 433–449.
- [2] S.M. Tikoo, A.J. Evans, *Dynamos in the inner solar system*, *Annu. Rev. Earth Planet. Sci.* 50 (1) (2022) 99–122.
- [3] C.L. Johnson, et al., Crustal and time-varying magnetic fields at the InSight landing site on Mars, *Nat. Geosci.* 13 (3) (2020) 199–204.
- [4] D. Banfield, J.A. Rodriguez-Manfredi, C.T. Russell, K.M. Rowe, D. Leneman, H.R. Lai, et al., Insight auxiliary payload sensor suite (APSS), *Space Sci. Rev.* 215 (1) (2018) 4–33.
- [5] A. Mittelholz, et al., *J. Geophys. Res. Planets* 126 (11) (2021) e2021JE006980.
- [6] C.L. Johnson, et al., *Nat. Geosci.* 13 (3) (2020) 199–204.
- [7] P. Amaro, et al., Laser interferometer space antenna, 2017, <https://arxiv.org/abs/1702.00786>.
- [8] Armano, et al., Spacecraft and interplanetary contributions to the magnetic environment on-board LISA path-finder, *Mon. Not. R. Astron. Soc.* 494 (2) (2020) 3014–3027.
- [9] Aguilera, et al., STE-QUEST - test of the universality of free fall using cold atom interferometry, *Class. Quant. Grav.* 31 (11) (2014) 115010.
- [10] Q. Du, et al., Effect of magnetic flux modulation on noise characteristics of tunnel magnetoresistive sensors, *Appl. Phys. Lett.* 116 (10) (2020) 102405.
- [11] Q. Du, et al., High efficiency magnetic flux modulation structure for magnetoresistance sensor, *IEEE Electron. Dev. Lett.* 40 (11) (2019) 1824–1827.
- [12] W. Tian, et al., Magnetic flux vertical motion modulation for $1/f$ noise suppression in magnetoresistance field sensors using MEMS device, *IEEE Trans. Magn.* 52 (2) (2013) 1–6.
- [13] X. Li, et al., A novel high-precision digital tunneling magnetic resistance-type sensor for the nanosatellite space application, *Micromachines* 9 (3) (2018) 121.
- [14] Yuyu Hou, et al., A low $1/f$ noise tunnel magnetoresistance accelerometer, *IEEE Trans. Instrum. Meas.* 71 (2021) 9502511.
- [15] Haoqi Lyu, et al., A high-resolution MEMS magnetoresistive sensor utilizing magnetic tunnel junction motion modulation driven by the piezoelectric resonator, *Appl. Phys. Lett.* 121 (12) (2022).
- [16] Y. Xie, et al., Towards T2-limited dc diamond quantum magnetometry via flux concentration and modulation, *IEEE Sens. J.* (2023).
- [17] J. Sanjuán, et al., Thermal diagnostics front-end electronics for LISA pathfinder, *Rev. Sci. Instrum.* 78 (2007) 104904.
- [18] D. Roma-Dollase, et al., Resistive-based micro-kelvin temperature resolution for ultra-stable space experiments, *Sensors* 23 (1) (2023) 145.
- [19] Toda, et al., Cantilever beam temperature sensors for biological applications, *IEEE Trans.* 12 (2017) 153–160.
- [20] C. Lei, et al., Noise analysis and improvement of a micro-electro-mechanical-systems fluxgate sensor, *Measurement* 122 (2018) 1–5.
- [21] H. Nhalil, et al., Planar hall effect magnetometer with 5 pT resolution, *IEEE Sens. Lett.* 3 (2019) 1–4.
- [22] I. Mateos, M. Diaz-Aguiló, F. Gibert, I. Lloro, A. Lobo, M. Nofrarias, J. Ramos-Castro, Temperature coefficient improvement for low noise magnetic measurements in LISA, *J. Phys.: Conf. Ser.* 363 (2012) 012051.
- [23] M.D. Michelena, Commercial off-the-shelf GMR based sensor on board opto picosatellite, in: *Giant Magnetoresistance (GMR) Sensors, Smart Sensors, Measurement and Instrumentation*, Springer Berlin Heidelberg, Berlin, Heidelberg, 2013, pp. 181–210.
- [24] https://www.aecensors.com/components/com_virtuemart/shop_image/product/Magnetic-Tunnelling-Magnetoresistive-TMR-Linear-Sensors/pdfs/TMR9112-Datasheet-EN-V2.0a.pdf.
- [25] B.J. Anderson, M.H. Acuña, D.A. Lohr, J. Scheifele, A. Raval, H. Korth, J.A. Slavin, The magnetometer instrument on MESSENGER, *Space Sci. Rev.* 131 (1) (2007) 417–450, <http://dx.doi.org/10.1007/s11214-007-9246-7>.
- [26] S. Solomon, et al., The MESSENGER mission to mercury: Scientific objectives and implementation, *Planet. Space Sci.* 49 (14–15) (2001) 1445–1465.
- [27] C. Tao, F. Sahrroui, D. Fontaine, J. de Patoul, T. Chust, S. Kasahara, A. Retinò, Properties of Jupiter's magneto-spheric turbulence observed by the galileo spacecraft, *J. Geophys. Res. Space Phys.* 120 (4) (2015) 2477–2493, <http://dx.doi.org/10.1002/2014JA020749>.
- [28] M.P. de Souza Echer, E. Echer, M.O. Domingues, O. Mendes, R.T. Seo, W. Gonzalez, Wavelet analysis of low frequency magnetic field fluctuations in the Jupiter's magnetotail, *Adv. Space Res.* 68 (1) (2021) 246–258, <http://dx.doi.org/10.1016/j.asr.2021.03.003>.
- [29] M.G. Kivelson, et al., The Galileo magnetic field investigation, *Space Sci. Rev.* 60 (1992) 357–383.
- [30] D. Ulusen, et al., Solar control of the Martian magnetic topology: Implications from model-data comparisons, *Planet. Space Sci.* 128 (2016) 1–13.
- [31] C.T. Russell, R.C. Snare, J.D. Means, R.C. Elphic, Pioneer venus orbiter fluxgate magnetometer, *IEEE Trans. Geosci. Remote Sens.* GE-18 (1) (1980) 32–35, <http://dx.doi.org/10.1109/TGRS.1980.350256>.
- [32] R. Snare, et al., A magnetometer for the pioneer venus orbiter, *IEEE Trans. Magn.* 13 (5) (1977) 1107–1109.
- [33] R. Snare, et al., Measurement of instrument noise spectra at frequencies below 1 hertz, *IEEE Trans. Magn.* 9 (3) (1973) 232–235.
- [34] M. Nofrarias, F. Gibert, N. Karnesis, A.F. García, M. Hewitson, G. Heinzl, Danzmann K., Subtraction of temperature induced phase noise in the LISA frequency band, *Phys. Rev. D* 87 (2013) 102003, <http://dx.doi.org/10.1103/PhysRevD.87.102003>.
- [35] Y.-J. Min, et al., A CMOS magnetic hall sensor using a switched biasing amplifier, *IEEE Sens. J.* 12 (2012) 1195–1196.
- [36] A.V. Leonov, et al., A silicon field-effect hall sensor with an extended operating temperature range, *Instrum. Exp. Tech.* 59 (5) (2016) 724e727.
- [37] D. Novotny, et al., A digitally compensated AMR magnetometer, *IEEE Trans. Magn.* 55 (2019) 1–5.
- [38] P. Ripka, Improving the accuracy of magnetic sensors, *Sensors* (2008) 45e60.
- [39] https://www.nve.com/Downloads/analog_catalog.pdf.

- [40] H.-F. Liu, et al., A review of high-performance MEMS sensors for resource exploration and geophysical applications, *Pet. Sci.* 19 (2022) 2631–2648.
- [41] L. Gao, et al., High-precision acceleration measurement system based on tunnel magneto-resistance effect, *Sensors* 20 (1117) (2020).
- [42] H. Lyu, et al., A high-resolution MEMS magnetoresistive sensor utilizing magnetic tunnel junction motion modulation driven by the piezoelectric resonator, *Appl. Phys. Lett.* 121 (2022) 123504.
- [43] J. Odom, et al., The MAVEN magnetic field investigation, 2014.
- [44] S. Ruhunusiri, et al., Characterization of turbulence in the mars plasma environment with MAVEN observations, *J. Geophys. Res. Space Phys.* 122 (1) (2017) 656–674.
- [45] C.T. Russell (Ed.), *The Mars Plasma Environment*, Springer Science & Business Media, 2010.
- [46] J.R. Espley, et al., Observations of low-frequency magnetic oscillations in the Martian magnetosheath, magnetic pileup region, and tail, *J. Geophys. Res. Space Phys.* 109 (A7) (2004).
- [47] C.T. Russell (Ed.), *The Cassini-Huygens Mission: Orbiter in Situ Investigations*, Vol. 104, Springer Science & Business Media, 2005.
- [48] G. Kleindienst, et al., Quasiperiodic ULF-pulsations in saturn's magnetosphere, in: *Annales Geophysicae*, Vol. 27, (2) Copernicus Publications, Göttingen, Germany, 2009, pp. 885–894.
- [49] P. Dyal, et al., Lunar surface magnetometers, *IEEE Trans. Magn.* 9 (3) (1973) 226–231.
- [50] P. Dyal, et al., Lunar surface magnetometer, *IEEE Trans. Geosci. Electron.* 8 (4) (1970) 203–215.